

Design and development of a hand-held optical probe toward fluorescence diagnostic imaging

Bhavani Jayachandran

Jiajia Ge

Steven Regalado

Anuradha Godavarty

Florida International University

Optical Imaging Laboratory

Department of Biomedical Engineering

Miami, Florida 33174

E-mail: godavart@fiu.edu

Abstract. Near-infrared optical imaging is an emerging noninvasive technology toward breast cancer diagnosis. The optical imaging systems available to date are limited either by flexibility to image any given breast volume, patient comfort, or instrument portability. Here, a hand-held optical probe is designed and developed, 1. employing a unique measurement scheme of simultaneous multiple point illumination and collection for rapid data acquisition and minimal patient discomfort, and 2. employing a curved probe head such that it allows flexible imaging of tissue curvatures. Simulation studies are carried out on homogeneous slab phantoms ($5 \times 10 \times 8$ cc) to determine an appropriate source-detector configuration for the probe head. These design features are implemented in the development of the probe, which consisted of six simultaneous illuminating and 165 simultaneous collecting fibers, spaced 0.5 cm apart on a 5×10 sq-cm probe head. Simulation studies on 3-D slab and curved phantoms demonstrate an increase in the total area of predicted fluorescence amplitude and overall signal strength on using simultaneous multiple point sources over a single point source. The probe is designed and developed such that on coupling with a detection system in the future, the hand-held probe based imager can be clinically assessed toward cancer diagnostic imaging. © 2007 Society of Photo-Optical Instrumentation Engineers. [DOI: 10.1117/1.2799193]

Keywords: optical imaging; fluorescence contrast agents; hand-held probe; intensified charge-coupled device camera; frequency domain; breast cancer.

Paper 06354R received Nov. 30, 2006; revised manuscript received May 2, 2007; accepted for publication May 31, 2007; published online Oct. 24, 2007.

1 Introduction

Over the past few years, several laboratories have embarked on the development of fluorescence-enhanced optical imaging as a new modality for molecularly based diagnostic imaging in deep tissues, particularly in the female breast.¹⁻¹⁴ Fluorescence-enhanced optical imaging involves the use of near-infrared (NIR) light and external contrast agents to enhance the optical contrast between normal and diseased tissue regions, and thus molecularly target the metastatic cancer cells within the breast tissue.

Various investigators employ different source-detector imaging configurations during the development of their fluorescence-enhanced or nonfluorescence-based optical imaging systems. These imaging configurations can be broadly classified into^{15,16}: 1. compressed tissue-based configuration, 2. circular configuration, and 3. subsurface configuration (Fig. 1). To date, most 3-D optical imaging studies toward breast cancer diagnosis are restricted either to compressed tissue configuration^{7,10,17-20} [Fig. 1(a)] or circular configuration^{5,6,8,21-27} [Fig. 1(b)]. The compressed tissue configuration is analogous to x-ray mammography, and is disadvantageous due to minimal patient comfort from tissue com-

pression and limited information obtained around the complete breast tissue. The circular configuration has minimal patient discomfort, but is limited by the bulky and nonportable instrumentation. Subsurface configuration [Fig. 1(c)] is a relatively new method that requires no tissue compression, and can be designed to mimic a portable and flexible imaging probe.²⁸⁻³⁵ However, 3-D tomography studies using the subsurface imaging configuration are limited³⁶⁻³⁸ and challenging due to limited depth information obtained using only reflectance-based measurements during imaging reconstructions. In addition, the hand-held-based imaging systems (employing the subsurface imaging configuration) developed to date are typically designed to image flat surfaces^{28-30,33-35} and are not entirely adaptable to tissue curvatures.

These source-detector imaging configurations can be implemented using one of the measurement geometries (Fig. 2), which include: 1. sequential single-point illumination and sequential/simultaneous multiple-point collection using optical fibers,^{4,5,9,11,39-46} 2. simultaneous multiple point illumination and simultaneous multiple point collection using optical fibers,^{12,43} and 3. area illumination and area detection using an expanded beam of excitation source and a charge-coupled device (CCD) camera,^{38,41,45} respectively. To date, most fluorescence optical tomographic studies have been typically per-

Address all correspondence to Anuradha Godavarty, Dept. of Biomedical Engineering, Florida International University, EC 2675-10555 W Flagler St, Miami, FL 33174. Tel: 305-348-7340; Fax: 305-348-6954; E-mail: godavart@fiu.edu

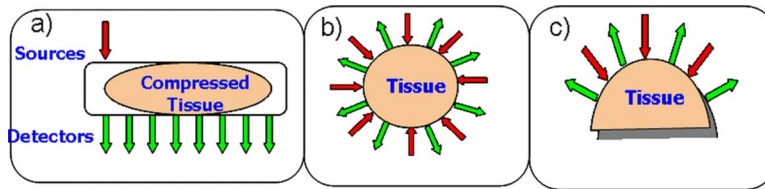


Fig. 1 Different imaging configurations: (a) compressed tissue configuration, (b) circular imaging configuration, and (c) subsurface imaging configuration. (Adapted from Ref. 16)

formed using sequential multiple point illumination and sequential^{7,18} or simultaneous^{5,8,21,22,47–50} multiple point collection measurement geometries obtained with or without the use of optical fibers.^{11,23–25,40,49,51,52} While the data acquisition rates improve on using simultaneous multiple point collection techniques, sequential multiple point illumination not only impacts the total imaging time, but may also provide insufficient light intensity to perform tomographic studies on large tissue volumes with greater penetration depth (since optical signals decay exponentially with distance). Weak optical signals are usually dominated by noise, thus impacting the measurement precision and accuracy, and eventually hindering the accurate reconstruction of the target location and size.

Recently, Godavarty et al.⁴³ employed the simultaneous multiple (dual) point illumination-based measurement geometry toward fluorescence tomography studies on large breast phantoms, and successfully demonstrated 3-D image reconstructions under various experimental conditions. From these studies, it was also demonstrated that simultaneous multiple point illumination provided: 1. an increase in the total area of fluorescence amplitude on the imaging surface; 2. higher signal strength; 3. an increase in the total number of measurements (therefore decreased data acquisition time); and 4. a decrease in the measurement error (i.e., error between repeated measurements) and model mismatch error (i.e., error between experimental and simulated measurements); in comparison to using sequential single point illumination geometry.

In this study, we designed and developed a hand-held-based optical probe with a subsurface imaging configuration and simultaneous illumination and detection-based measurement geometry, such that the probe allows flexible imaging of any tissue curvature (obtained using both reflectance and tran-

sillumination measurements) with improved signal strength and enhanced data acquisition rates. Simulation studies were performed to determine the appropriate number of simultaneous illuminating sources and their layout on the optical probe head. The effect of simultaneous multiple point illumination over single point illumination was determined in terms of the overall signal strength, total area of fluorescence amplitude, and tissue curvature. A design was implemented to simultaneously illuminate multiple point sources from a single laser diode point source. The design and development of the hand-held-based optical probe is described in the following sections.

2 Materials and Methods

The hand-held optical probe was designed using a subsurface imaging configuration and simultaneous multiple point illumination and collection based measurement geometry. The design was further implemented toward the development of the optical probe with a geometrically adaptive probe head that allows imaging of any given tissue curvature (up to 45-deg) with good probe-tissue contact and minimal patient discomfort.

Design of the hand-held probe was carried out as a two-fold process: 1. design the appropriate illumination-collection fiber layout and number on the probe head; and 2. design a unique technique to simultaneously illuminate multiple sources and also be able to image tissue curvatures. Simulated studies were also carried out on the developed probe, to study the effect of introducing curvature on simultaneous illumination and collection.

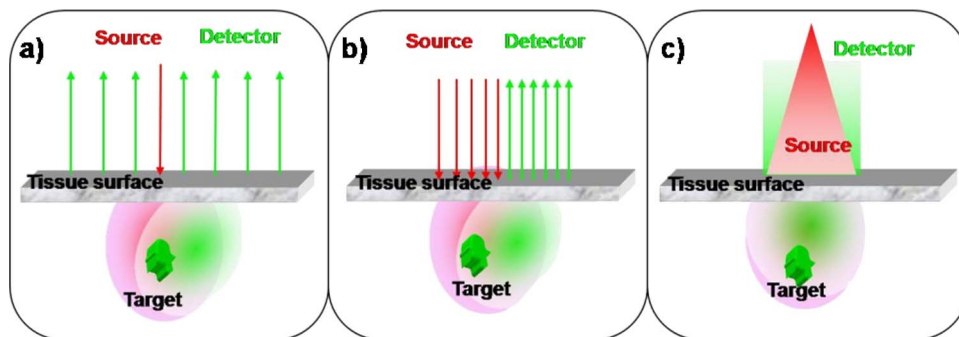


Fig. 2 Different measurement geometries: (a) sequential single point illumination and sequential/simultaneous multiple point collection using optical fibers; (b) simultaneous multiple point illumination and simultaneous multiple point collection using optical fibers; and (c) area illumination and area detection using an expanded beam of excitation source and a CCD camera, respectively. (b) and (c) are equivalent, if each point of area illumination is assumed as an individual optical fiber.

Table 1 The optical properties of the homogeneous phantom(s) with fluorophore used in the forward-model-based simulation studies. μ_{ax} : absorption coefficient at excitation wavelength. μ_{am} : absorption coefficient at emission wavelength. μ'_{sx} : reduced scattering coefficient at excitation wavelength. μ'_{sm} : reduced scattering coefficient at emission wavelength. ϕ : quantum efficiency of ICG. τ : lifetime of ICG.

μ_{ax} (cm ⁻¹)	μ_{am} (cm ⁻¹)	μ'_{sx} (cm ⁻¹)	μ'_{sm} (cm ⁻¹)	ϕ	τ (nsec)
0.02483	0.0322	10.879	9.8241	0.01088	0.56

2.1 Design of Illumination-Collection Fiber Layout and Number on the Probe Head

An appropriate number and distribution of the simultaneous illuminating and collecting optical fibers is essential to maximize the total area of fluorescence amplitude, minimize the regions with very weak or no fluorescence optical signals (hereafter termed as *dead regions*), and enhance the signal strength. A rectangular probe head of 5×10 cm² dimensions was chosen, keeping in mind the typical dimensions of breast tissue (further details are provided in Sec. 2.2.1). Simulation studies were carried out on a 3-D homogeneous phantom of $5 \times 10 \times 8$ cm³ dimensions, with the imaging surface as 5×10 cm² at $z=0$ cm plane. The phantom depth was chosen as 8 cm (in the z direction) to represent the infinite boundary in the z direction, thus mimicking the extended chest wall regions of the breast tissue.

2.1.1 Finite-element-based simulation studies

Simulation studies were carried out by solving the forward model of the coupled diffusion equations,⁵²⁻⁵⁴ where the fluorescence optical properties of the phantom are assumed to be known *a priori* and the fluence of the emitted fluorescence signal is determined using the Galerkin approximation of the finite-element-based numerical technique.⁵⁵ Coupled diffusion equations in the frequency domain were applied in these simulation studies, since the hand-held optical probe devel-

oped will be coupled to a gain-modulated intensified CCD (ICCD) detection system toward the development of a frequency-domain-based optical imaging system (future work for experimental studies).

Initially, a 3-D homogeneous finite element mesh containing tetrahedral elements was generated using Gambit 2.1.6 (Fluent Incorporated, Lebanon, New Hampshire) software to perform simulated studies on slab phantoms of $5 \times 10 \times 8$ cm³ dimensions. The mesh was discretized into 19,267 tetrahedral elements and 4017 nodes, with 0.5-cm spacing between nodes on the imaging surface. The imaging surface (at $z=0$ cm) consisted of 3034 triangular elements and 231 nodes, where each node was assumed to be either an illuminating or collecting point location on the probe head. The homogeneous optical properties of the phantom chosen for these simulation studies were similar to those used in experimental breast phantom studies⁹ and are given in Table 1. The fluorophore used in all the simulation studies was indocyanine green (ICG), which was assumed to be uniformly distributed in the homogeneous phantoms.

The finite-element forward simulator developed using the adjoint method⁵⁵ was adapted for the current studies and implemented using Matlab V.6.5 (Mathworks Incorporated, Natick, Massachusetts). The predicted emission fluence [$\Phi = AC \exp(i\theta)$] at each node on the imaging plane was in turn used to calculate the amplitude (AC) and phase shift (θ) of the emitted fluorescence signal. Simulations were carried out for two different scenarios: 1. changing the number of simultaneously illuminating sources (1, 3, 5, 6, and 8) and the distance between them; and 2. changing the layout of the illuminating point sources, to maximize the total area of predicted fluorescence amplitude on the imaging surface as well as improve the overall signal strength. The different number of simultaneous illuminating point sources used in the simulation studies and their locations on the imaging plane are as shown in Fig. 3.

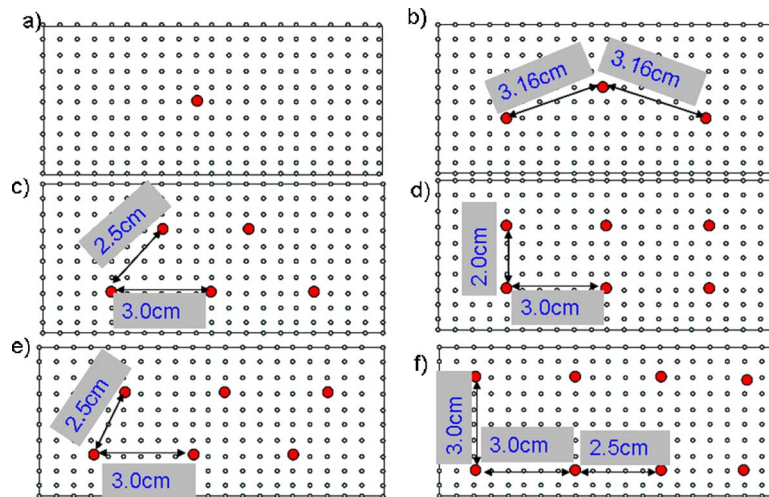


Fig. 3 The illuminated/detected surface on the $5 \times 10 \times 8$ -cm³ phantom, where the solid red circles represent the point source(s) and the hollow black circles represent the point detectors for the following cases: (a) single point illumination, (b) simultaneous three point illumination, (c) simultaneous five point illumination, (d) simultaneous six point illumination, (e) simultaneous six point illumination with a different layout, and (f) simultaneous eight point illumination (Color online only.)

Table 2 Normalizing techniques for calculating areas of predicted fluorescence amplitude and comparing signal strength between simultaneous multiple point illumination and single point illumination. AC_{Tmax} corresponds to the larger intensity of AC_{mmax} and AC_{smax} , where suffix *max* is the maximum fluorescence amplitude intensity for the given case (i.e., multiple sources or single source case).

	Method 1: to compare signal strength	Method 2: to calculate area of predicted AC
Multiple sources (suffix m)	AC_m/AC_{Tmax}	AC_m/AC_{mmax}
Single source (suffix s)	AC_s/AC_{Tmax}	AC_s/AC_{smax}

2.1.2 Data analysis procedures

Fluorescence amplitude measurements (AC) of the emitted NIR signal obtained from simulation studies were used to study the effect of simultaneous multiple point illumination over single point illumination on the overall signal strength and total area of predicted AC . These predicted AC measurements were normalized and presented as 2-D surface contour plots using Tecplot 11.0 (Tecplot, Incorporated, Bellevue, Washington). The simulated fluorescence amplitude point measurements were normalized differently for evaluating the signal strength and the total area of predicted AC on the imaging surface, as described in Table 2. To qualitatively compare the effect of using simultaneous multiple point sources over single point illumination on the overall signal strength, the emitted fluorescence amplitude for both source illumination cases was normalized with the maximum fluorescence amplitude between the two source illumination cases (see Table 2, method 1). In quantifying the total area of predicted AC on the imaging surface, the emitted fluorescence amplitude at each nodal point of the finite-element mesh was normalized by the maximum fluorescence amplitude for the given source illumination used (see Table 2, method 2). A cutoff value of $\sim 20\%$ of the maximum fluorescence amplitude (i.e., 0.2 in the normalized fluorescence amplitude) was chosen to differentiate between signal and background noise. Various cutoff values have been attempted (5, 10, 15, and 20%). However, 20% was chosen for our studies in an attempt to maximize noise reduction in the measured signal (keeping in mind the future experimental studies). Thus only AC values $\geq 20\%$ of the maximum AC (i.e., 0.2 and above in the normalized fluorescence amplitude) were used in evaluating the total area of predicted AC in each simulated case, using interpolation techniques available as built-in functions in the Tecplot software.

The quantified area of predicted AC was in turn used to determine the appropriate: 1. distance between simultaneous

multiple point sources; 2. number of simultaneous multiple point sources; and 3. source fiber layout; such that this total area of predicted AC on the imaging surface is maximized.

2.2 Design of Simultaneous Illumination and Curvature of the Probe Head

2.2.1 Simultaneous illumination technique

Simultaneous multiple point illumination with sources of equal intensity can be made possible using either: 1. multiple 50:50 and/or 70:30 beamsplitters (assembled in a housing) that is used to split the incident NIR light from the laser diode into multiple beams; or 2. an expanded laser beam focused on a fiber bundle that holds multiple optical fibers. In this study, the expanded laser beam configuration was chosen due to the simplicity of the product design, although it is challenging to obtain equal intensities using this configuration.

Here, a six-legged (details in Sec. 3) fiber bundle (one end fused and the other end split into six individual fibers) of ~ 2 m was custom-built (Romack Incorporated, Williamsburg, Virginia) using 600- μm -diam multimode optical fibers (numerical aperture $NA=0.22$) (Fig. 4). The six legs of the fiber bundle were coupled onto the probe head at different point locations, based on the chosen source fiber layout (described in Sec. 3). The fused end of the fiber bundle was connected to a collimator-diffuser package to homogenize the input light source from the laser diode (Sanyo DL7140-201S model, Thorlabs, Incorporated, Newton, New Jersey) of 785-nm wavelength and 500-mW maximum power. A high-power laser diode was used in these studies, since the collimator-diffuser package tends to attenuate the incident laser source light significantly ($>90\%$). The intensity distribution of the laser source light among the six fibers (with and without the use of the collimator-diffuser package) was measured using an optical power meter (PM 100 model, Thorlabs Incorporated, Newton, New Jersey) to assess the effect of using the collimator-diffuser package.

A collection fiber bundle consisting of 165 multimode optical fibers (600 μm , $NA=0.22$) was also custom-built by Romack, Incorporated to collect the emitted NIR signal from the imaging surface. The 165 multimode fibers were fused onto a 2-in-diam ring, such that simultaneous detection of the emitted signal can be performed by coupling the bundle to an intensified charge-coupled device (ICCD)-based detection system.

2.2.2 Design of curvature onto the probe head

The probe head was designed such that it can adapt to any tissue curvature, thus improving the tissue-probe contact as well as obtaining better depth information (since transillumination measurements can be acquired apart from reflectance measurements). As a first-generation optical probe, the curva-

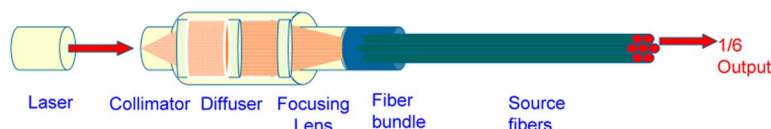


Fig. 4 Schematic of the six-legged illumination fiber bundle, where a collimator-diffuser package between the bundle and laser source will homogenize the light output more uniformly among the six fibers.

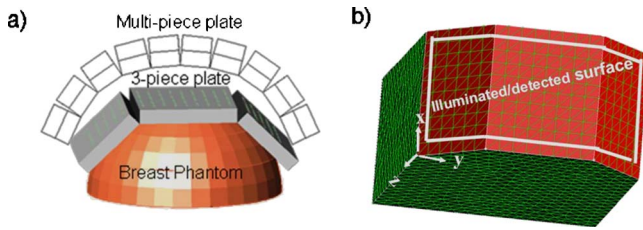


Fig. 5 (a) The first-generation three-piece plate-based probe design as a simplified version of the ideal case containing multiple face plates for better contact on the tissue curvature. (b) The finite element mesh of the same 3-D curved phantom. The curved phantom with 45-deg angle of curvature is similar to the one shown here.

ture in the probe head was introduced using three plates hinged together such that 0 to 45-deg flexibility was possible independently on each end plate, as shown in Fig. 5(a). Although increasing the number of face plates would increase the angle of curvature (approaching the curvature of the breast tissue), such an implementation is more challenging and will be attempted as a part of our next-generation hand-held optical probe.

The aluminum-based three-plate probe head was built at Florida International University's Manufacturing Research Center (FIU-MRC). The probe head was mounted on two railings for each end of the face plate, such that plates can be flexibly moved from 0 to 45-deg [Fig. 5(a)]. The movement and subsequent angle of curvature of each outer plate ($3 \times 5 \text{ cm}^2$) with respect to the center plate ($4 \times 5 \text{ cm}^2$) can be measured using an angular indicator consisting of notches at the edges of the railings.

2.3 Effect of Simultaneous Illumination on Curved Phantoms

The probe head's illumination-collection fiber layout and number was designed assuming that the probe was flat, i.e., no curvature. The effect of simultaneous multiple point illumination in terms of signal strength and area of predicted AC was studied on a slab phantom using the flat probe with 0-deg curvature. The curvature (0 to 45-deg) was introduced to the probe head using the design described before. To study the effect of simultaneous multiple point illumination on curved phantoms using the curved probe head, 3-D phantoms with 35- and 45-deg curvature on the imaging surface alone were generated [see Fig. 5(b)], such that the probe head has good surface contact with the imaging surface. The curved phantoms were generated with similar dimensions as the 3-D slab phantom (described in Sec. 2.1), except that a curvature was introduced on the illuminated/detected surface in concurrence with the design of the three-piece probe head.

2.3.1 Forward simulation on curved phantoms

Three-dimensional homogeneous finite element meshes containing tetrahedral elements were generated using Gambit 2.1.6 software for both the curved phantoms [see Fig. 5(b)], and the mesh details are provided in Table 3. The illumination/detected surface consists of 3034 elements and 231 nodes, six of which are considered as point source locations and the remaining as point detector locations. The homogeneous optical properties of the phantom were similar to

Table 3 Finite element mesh details of the 3-D curved phantoms.

Phantom number	Type	Nodes	Elements
1	Curved (35-deg)	4523	25179
2	Curved (45-deg)	3976	22126

that used in previous simulation studies on slab phantoms (Sec. 2.1). The predicted fluorescence amplitude measurements (AC) of the emitted NIR signal were evaluated on the imaging surface of two curved phantoms for both the single point illumination and simultaneous six point illumination geometry, to study the effect of simultaneous multiple point illumination on the total area of predicted AC on the imaging surface and the overall signal strength.

The data analysis procedure was similar to that used in the slab phantom simulation studies (see Sec. 2.1.2). Two-dimensional surface contour plots of normalized emitted fluorescence amplitude data from curved phantom studies were generated by similar methods described in Table 2, except that the curved imaging surface was projected onto a 2-D plane of equivalent dimensions (i.e., $5 \times 10 \text{ cm}^2$).

3 Results and Discussions

3.1 Illumination-Collection Fiber Layout on Probe Head

Simulated 3-D slab phantom studies were performed using simultaneous multiple point illumination geometry applying: 1. a different number of simultaneous multiple point sources (1, 3, 5, 6, and 8); and 2. different source fiber layouts. The 2-D surface ($5 \times 10 \text{ cm}^2$) contour plots of the emitted fluorescence amplitude at $z=0\text{-cm}$ plane (i.e., imaging surface) were plotted for the different number of simultaneous multiple point sources as shown in Fig. 6. The total area of predicted AC increased with an increase in the number of simultaneous point sources (see Fig. 7). It was observed that the total area of predicted AC was greater than the product of the area of predicted AC for single point illumination (i.e., 3.9 cm^2) and the total number of sources, until up to six simultaneous sources ($3.9 \text{ cm}^2 * 6 < 27.67 \text{ cm}^2$), thus improving the overall area of predicted fluorescence amplitude. When the number of simultaneous point sources was increased to eight, the total area of predicted AC was observed to be less than the product of the area for single point illumination and the number of sources ($3.9 \text{ cm}^2 * 8 > 31.05 \text{ cm}^2$). This indicated that an increase in the area of predicted AC was approaching a saturation point. In other words, a further increase in the number of sources did not significantly increase the total area of predicted AC for the given imaging surface. Hence, six simultaneous point sources were chosen as the appropriate number for our hand-held probe design. In addition, it was observed that changing the layout of these six simultaneous point sources (i.e., changing the distance between these point sources) affected the total area of predicted AC and overall signal strength, as shown in Fig. 8. These 2-D surface contour plots of the emitted fluorescence amplitude for different source fiber layouts demonstrate an increase in the total area of predicted AC using the layout given in Fig.

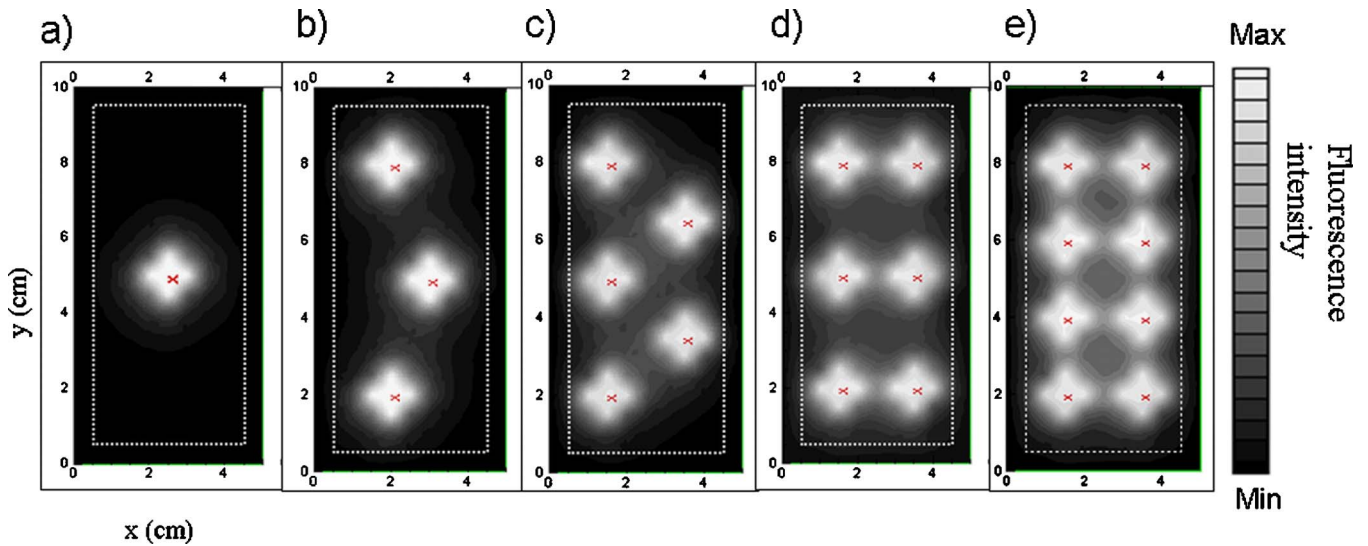


Fig. 6 Two-dimensional surface contour plots of the simulated fluorescence amplitude on the illuminated/detected surface of 3-D slab phantoms at $z=0$ -cm plane. The simulations were carried out for homogeneous phantoms of uniform fluorescence light distribution using (a) single point illumination, (b) simultaneous three point illumination, (c) simultaneous five point illumination, (d) simultaneous six point illumination, and (e) simultaneous eight point illumination-based measurement geometry. The red “x” signs are the x-y locations of the point sources. The dashed white line (of $9 \times 4 \text{ cm}^2$) represents the actual region within which the illuminating and collection fibers were placed on the developed hand-held probe. (Color online only.)

8(c), compared to the layouts shown in Figs. 8(a) and 8(b). In addition, the overall signal strength improved with the appropriate choice of the source fiber layout [Fig. 8(c)], as shown quantitatively at a single randomly chosen point in the contour plots. Based on these observations, the source fiber layout shown in Fig. 8(c) (distance between sources was ~ 2.5 to 3.0 cm) was chosen as an appropriate layout to be implemented toward the development of the optical probe head.

3.2 Effect of Simultaneous Illumination on Curved Phantom

Simulated 3-D curved phantom studies were performed using single point illumination geometry and simultaneous six point illumination geometry on 35- and 45-deg curved phantoms, respectively. The 2-D surface contour plots of emitted fluorescence amplitude from the curved surface of each curved

phantom are presented on a projected imaging plane of $5 \times 10 \text{ cm}^2$, as shown in Fig. 9. From these surface contour plots (Fig. 9), it was observed that simultaneous multiple point illumination enhanced the overall signal strength and the total area of predicted AC on the imaging plane in comparison to the single point illumination for both the curved phantoms. However, the increase in both these parameters was less for curved phantoms in comparison to that for slab phantoms (with no curvature), as observed from Figs. 9(a), 9(c), and 8(c), respectively.

Unlike the symmetric distribution of fluorescence intensity on the imaging plane of the slab phantom (with 0-deg curvature), the curved phantoms generate an irregular distribution of the emitted fluorescence signal (especially at the two end plates of $3 \times 5 \text{ cm}^2$ each) and a decreased total area of predicted AC [see Figs. 9(a) and 9(c)]. This phenomenon could possibly be due to a decrease in the fluorescence intensity at

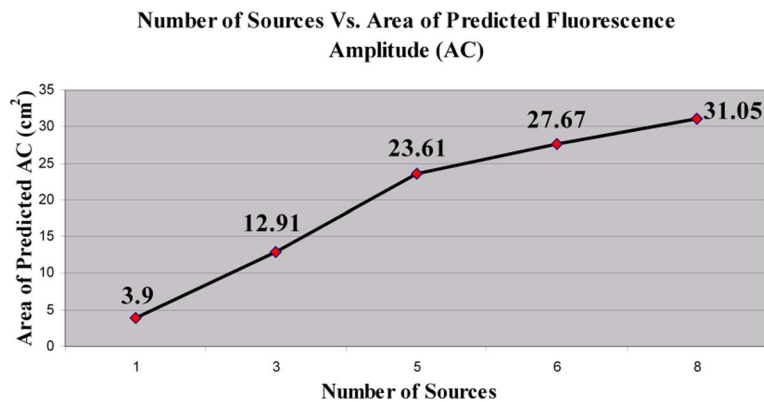


Fig. 7 A plot of the total area of predicted fluorescence amplitude versus number of simultaneous sources for simulated studies on 3-D slab phantoms.

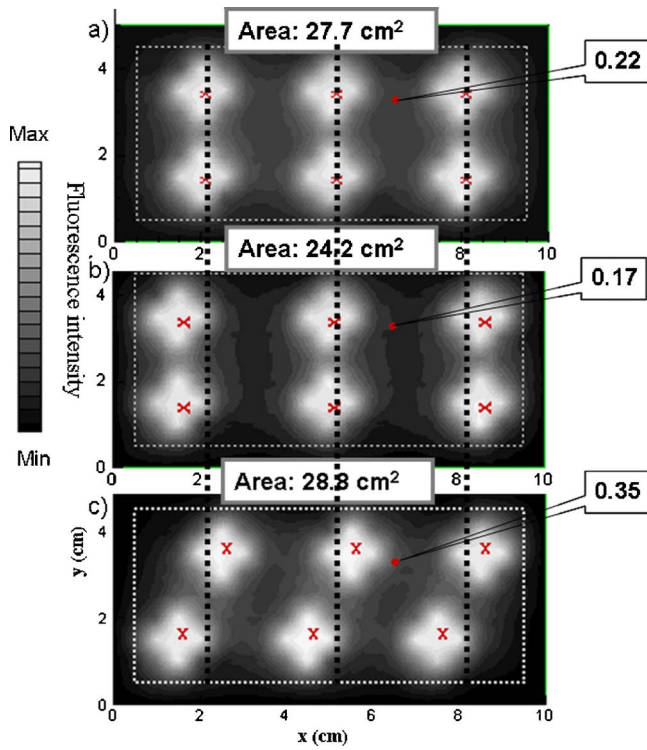


Fig. 8 Two-dimensional surface contour plots of simulated fluorescence amplitude on the illuminated/detected surface of 3-D slab phantoms at $z=0$ -cm plane. The simulations were carried out for homogeneous phantoms of uniform fluorescence light distribution using different layouts (a), (b), and (c) of simultaneous six point sources.

the detectors in the null plane, from constructive interference of simultaneous multiple point sources that are in-phase.^{56,57} The constructive interference pattern for the three different phantoms can be observed (see Fig. 10) from the 2-D contour slice at $x=1.9$ -cm plane (chosen randomly). This interference causes a decrease in fluorescence amplitude at a few locations on the imaging surface, which in turn affects the total area of predicted AC for curved phantom(s) in comparison to slab phantoms (no curvature) for a given multiple point source illumination geometry.

The source-separation distance is also a crucial factor for determining interference effects, which becomes less pronounced as the distance between two simultaneous point sources is ≥ 4 cm.⁵⁶ As shown in Fig. 10, the source-separation distance for the curved probe head was reduced from 3 cm on the flat imaging surface to 2.9 cm for 35-deg curvature and 2.8 cm for 45-deg curvature, allowing a greater interference between input light sources. The different source-separation distances, i.e., 3.0 and 2.9 cm for 35-deg curvature, of the curved phantom may explain the irregular signal distribution at two sides (or end plates), while the slab phantom, which has equal distance of source-separation (3 cm), was able to produce symmetric surface contour results. Apart from the source-separation distance, the curvature tends to play a significant role in the interference pattern, and in turn on the total surface area, of the predicted AC. In other words, a source-separation distance of 2.8 or 2.9 cm on a flat phantom (i.e., 0-deg curvature) will have less interference effect in comparison to the same source-separation distance on a curved phantom (i.e., >0 -deg curvature on the imaging surface).

In summary, there is still a positive impact of employing simultaneous multiple point illumination when imaging tis-

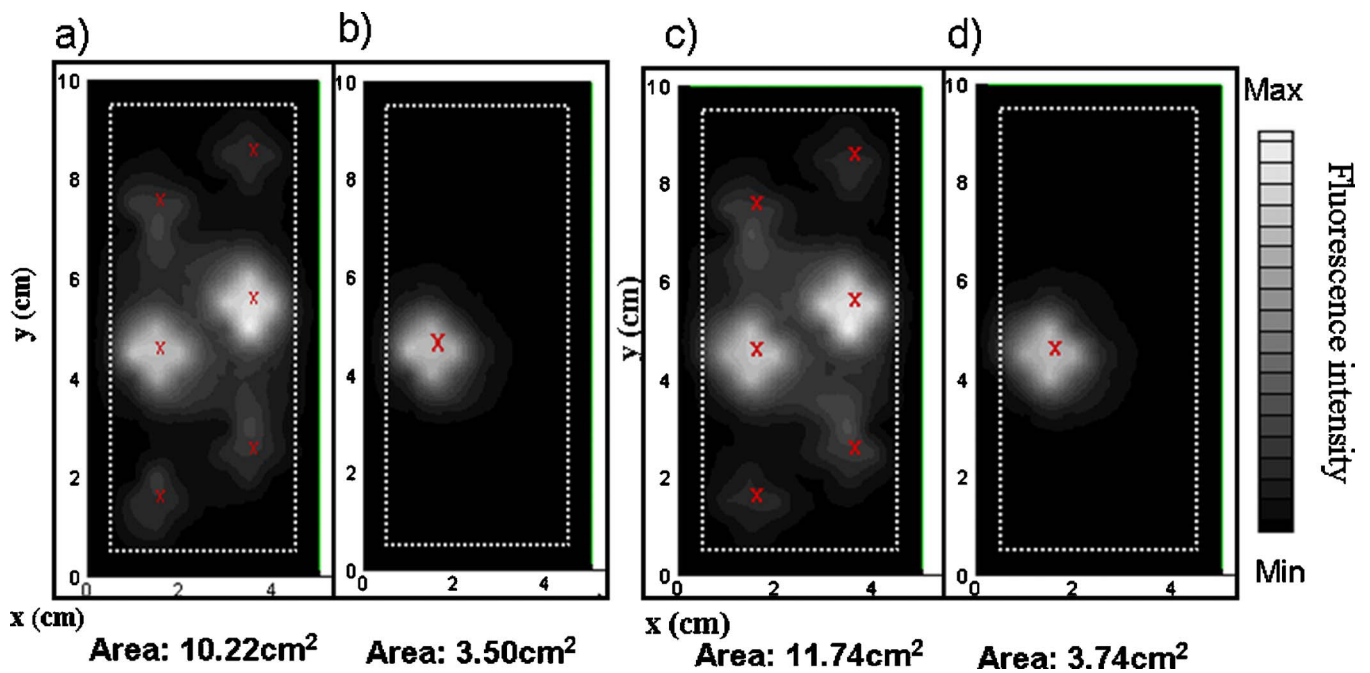


Fig. 9 Two-dimensional surface contour plots of simulated fluorescence amplitude on the illuminated/detected surface of 3-D curved phantoms. The simulations were carried out for homogeneous phantoms of uniform fluorescence light distribution using (a) and (c) simultaneous six point illumination, and (b) and (d) single point illumination on (a) and (b) 35-deg and (c) and (d) 45-deg based 3-D curved phantoms.

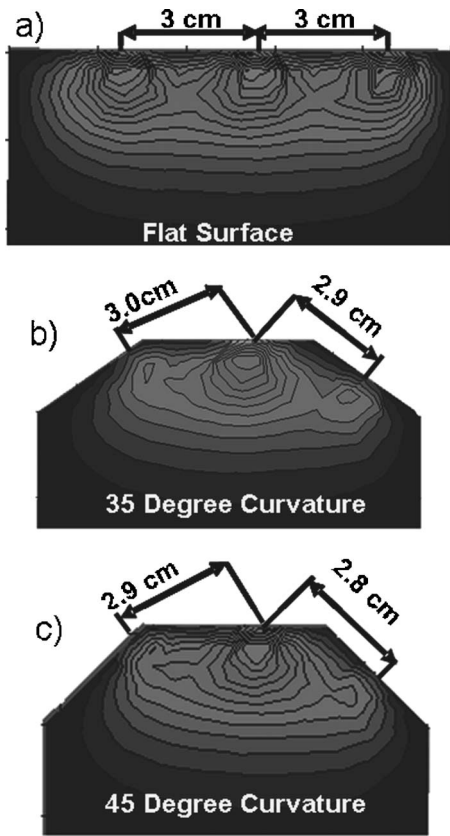


Fig. 10 Two-dimensional contour plots of simulated fluorescence amplitude in the (a) slab phantom, (b) 35-deg based curved phantom, and (c) 45-deg based curved phantom at $x=1.9$ -cm plane, using simultaneous six point illumination geometry.

sues of any given curvature at the imaging surface.

3.3 Developed Hand-Held-Based Optical Probe

Based on the simulation studies to design the appropriate illumination-collection fiber layout and number, along with the design of a simultaneous illumination technique and the curvature on the probe head, the hand-held-based optical probe was developed in our Optical Imaging Laboratory (see Fig. 11). The different components of the optical probe that were assembled together include the illumination and collec-

tion fiber bundles, three-plate probe head, and a railing system for introducing curvature (between 0 and 45-deg) during imaging.

The distance between collection fibers was chosen as 0.5 cm between each fiber due to practical limitations in trying to place the fibers closer.⁹ The fiber locations superimpose the nodes on the imaging surface of the 3-D phantom mesh. However, unlike in simulation studies where a total of 225 nodes represents the points of detection on the imaging surface (as described in Secs. 2.1.1 and 2.3.1), the actual probe consisted of only 165 collection points, assuming no fibers were located at the edges of the hand-held probe.

3.3.1 Effect of collimator-diffuser package on source intensity distribution

The source intensity distribution among the six legs of the illumination fiber bundle was determined with and without the use of the collimator-diffuser package. In the absence of the collimator-diffuser package, the output intensities among the six fibers varied significantly (~99.2% error difference). However, by using the collimator-diffuser package, the output intensity distribution among the fibers improved significantly (~19% error difference), although the collimator-diffuser package caused greater attenuation (~97%) of the input laser signal (maximum power of 500 mW). This indicates that a collimator-diffuser package is necessary to obtain uniform intensity distribution among simultaneous illuminating fibers. However, the losses due to this package are further evaluated (currently) to minimize the huge intensity losses through the package, and also make the intensity distribution more uniform among the six fibers.

In the future, the fused end of the collecting fiber bundle will be coupled to the focusing lens of the detection system and the final setup will be a unique hand-held-based optical imager that will be implemented toward flexible imaging of any tissue volume and curvature using a rapid data acquiring ICCD detection system.

4 Conclusion

The current work represents for the first time an optical probe development with the unique features of: 1. flexibility to image tissue curvatures (0 to 45-deg) that provides transillumination as well as reflectance measurements; 2. the ability to

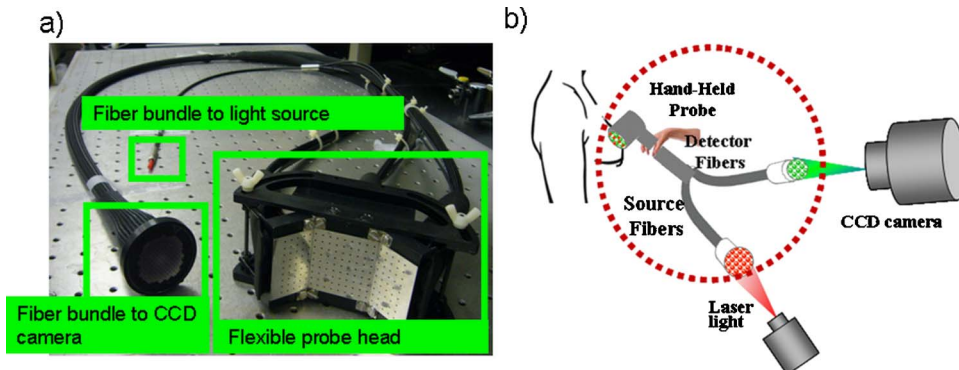


Fig. 11 (a) The developed hand-held-based optical probe with (b) future focus in developing a hand-held-based optical imaging system toward breast cancer diagnostic imaging.

simultaneously illuminate (at six point locations) and collect NIR signals (at 165 point locations) for rapid data acquisition; and 3. is a portable and comfortable hand-held design with good tissue contact and minimal patient discomfort.

An ideal hand-held optical fiber probe for clinical diagnostic studies is the area illumination and area detection measurement geometry [Fig. 2(c)], since the geometry mimics the clinically available ultrasound imaging probe. However, a more practical first step toward this ideal measurement geometry is the simultaneous multiple point illumination and multiple point collection measurement geometry, where each point of illumination/collection in the area illumination/collection geometry is assumed as an individual optical fiber that illuminates/collects the NIR signals.

Research is currently being performed at our Optical Imaging Laboratory to couple this hand-held-based optical probe to a time-dependent (frequency-domain) ICCD detection system and obtain tomographically meaningful experimental measurements on 3-D flat and curved phantoms (homogeneous and heterogeneous). Successful demonstration of 3-D tomographic imaging of large and curved phantoms using the hand-held-based optical imager will lead to its evaluation as a diagnostic and prognostic tool for breast cancer.

Acknowledgments

Godavarty would like to acknowledge the partial funding support from a Faculty Research Enhancement Award 2005 at Florida International University and Florida Department of Health (06BB-08).

References

1. E. M. Sevick-Muraca, A. Godavarty, J. P. Houston, A. B. Thompson, and R. Roy, "Near-infrared imaging with fluorescent contrast agents," in *Handbook of Biomedical Fluorescence*, Brian W. Pogue and Mary-Ann Mycek, Eds., Marcel Dekker Inc., New York (2003).
2. M. A. O'Leary, D. A. Boas, B. Chance, and A. G. Yodh, "Reradiation and imaging of diffuse photon density waves using fluorescent inhomogeneities," *J. Lumin.* **60**, **61**, 281–286 (1994).
3. J. Chang, R. L. Barbour, H. Graber, and R. Aronson, "Fluorescence optical tomography," *Proc. SPIE* **2570**, 59–72 (1995).
4. J. Wu, Y. Wang, L. Perleman, I. Itzkan, R. R. Dasari, and M. S. Feld, "Time-resolved multichannel imaging of fluorescent objects embedded in turbid media," *Opt. Lett.* **20**, 489–491 (1995).
5. V. Ntziachristos and R. Weissleder, "Experimental three-dimensional fluorescence reconstruction of diffuse media by use of a normalized Born approximation," *Opt. Lett.* **26**, 893–895 (2001).
6. Y. Yang, N. Ifimia, Y. Xu, and H. Jiang, "Frequency-domain fluorescent diffusion tomography of turbid media and in vivo tissues," *Proc. SPIE* **4250**, 537–545 (2001).
7. M. J. Eppstein, D. J. Hawrysz, A. Godavarty, and E. M. Sevick-Muraca, "Three-dimensional near-infrared fluorescence tomography with Bayesian methodologies for image reconstruction from sparse and noisy data sets," *Proc. Natl. Acad. Sci. U.S.A.* **99**, 9619–9624 (2002).
8. V. Ntziachristos, C. Bremer, and R. Weissleder, "Fluorescence imaging with near-infrared light: new technological advances that enable in vivo molecular imaging," *Eur. Radiol.* **13**, 195–208 (2003).
9. A. Godavarty, M. J. Eppstein, C. Zhang, S. Theru, A. B. Thompson, M. Gurfinkel, and E. M. Sevick-Muraca, "Fluorescence-enhanced optical imaging in large tissue volumes using a gain modulated ICCD camera," *Phys. Med. Biol.* **48**, 1701–1720 (2003).
10. B. Milstein, J. J. Stott, S. Oh, D. A. Boas, R. P. Millane, C. A. Bouman, and K. J. Webb, "Fluorescence optical diffusion tomography using multiple-frequency data," *J. Opt. Soc. Am. A* **21**(6), 1035–1049 (2004).
11. S. V. Patwardhan, S. R. Bloch, S. Achilefu, and J. P. Culver, "Time-dependent whole-body fluorescence tomography of probe bio-distributions in mice," *Opt. Express* **13**(7), 2564–2577 (2005).
12. Y. Chen, X. Intes, and B. Chance, "Development of high-sensitivity near-infrared fluorescence imaging device for early cancer detection," *Biomed. Instrum. Technol.* **39**(1), 75–85 (2005).
13. A. T. Kumar, J. Skoch, B. J. Bacskai, D. A. Boas, and A. K. Dunn, "Fluorescence-lifetime-based tomography for turbid media," *Opt. Lett.* **30**(24), 3347–3349 (2005).
14. E. E. Graves, D. Yessayan, G. Turner et al., "Validation of in vivo fluorochrome concentrations measured using fluorescence molecular tomography," *J. Biomed. Opt.* **10**(4), 044019 (2005).
15. A. P. Gibson, J. C. Hebden, and S. R. Arridge, "Recent advances in diffuse optical imaging," *Phys. Med. Biol.* **50**(4), R1–43 (2005).
16. B. W. Pogue, T. O. McBride, U. L. Osterberg, and K. D. Paulsen, "Comparison of imaging geometries for diffuse optical tomography of tissue," *Opt. Express* **4**(8), 270–286 (1999).
17. S. Fantini, S. A. Walker, M. A. Franceschini, M. Kaschke, P. M. Schlag, and K. T. Moesta, "Assessment of the size, position, and optical properties of breast tumors in vivo by noninvasive optical methods," *Appl. Opt.* **37**, 1982–1989 (1998).
18. J. Lee and E. M. Sevick-Muraca, "3-D Fluorescence enhanced optical tomography using references frequency-domain photon migration measurements at emission and excitation measurements," *J. Opt. Soc. Am. A* **19**, 759–771 (2002).
19. V. Quaresima, S. J. Matcher, and M. Ferrari, "Identification and quantification of intrinsic optical contrast for near-infrared mammography," *Photochem. Photobiol.* **67**, 4–14 (1998).
20. X. Li, J. Culver, T. Durduran, B. Chance, A. G. Yodh, and D. N. Pattanayak, "Diffraction tomography with diffuse-photon density waves: clinical studies and background subtraction," in *Advances in Optical Imaging and Photon Migration*, OSA Publications, Orlando, FL (1993).
21. V. Ntziachristos and R. Weissleder, "Charge-coupled-device based scanner for tomography of fluorescent near-infrared probes in turbid media," *Med. Phys.* **29**, 803–809 (2002).
22. V. Ntziachristos, C. Bremer, C. Tung, and R. Weissleder, "Imaging cathepsin B up-regulation in HT-1080 tumor models using fluorescence-mediated molecular tomography (FMT)," *Acad. Radiol.* **9**(suppl 2), S323–S325 (2002).
23. R. B. Schulz, J. Ripoll, and V. Ntziachristos, "Noncontact optical tomography of turbid media," *Opt. Lett.* **28**(18), 1701–1703 (2003).
24. V. Ntziachristos, E. A. Schellenberger, J. Ripoll, D. Yessayan, E. Graves, A. Bogdanov, J. L. Josephson, and R. Weissleder, "Visualization of antitumor treatment by means of fluorescence molecular tomography with an annex V-Cy5.5 conjugate," *Proc. Natl. Acad. Sci. U.S.A.* **101**(33), 12294–12299 (2004).
25. R. B. Schulz, J. Ripoll, and V. Ntziachristos, "Experimental fluorescence tomography of tissues with noncontact measurements," *IEEE Trans. Med. Imaging* **23**(4), 492–500 (2004).
26. C. Bremer, V. Ntziachristos, B. Weitkamp, G. Theilmeyer, W. Heindel, and R. Weissleder, "Optical imaging of spontaneous breast tumors using protease sensing 'smart' optical probes," *Invest. Radiol.* **40**(6), 321–327 (2005).
27. S. B. Colak, D. G. Papaioannou, G. W. t'Hooft, M. B. van der Mark, H. Schomberg, J. C. J. Paasschens, J. B. M. Melissen, and N. A. A. J. van Asten, "Tomographic image reconstruction from optical projections in light-diffusing media," *Appl. Opt.* **36**, 180–213 (1997).
28. Q. Zhu, N. G. Chen, D. Q. Piao, P. Y. Guo, and X. H. Ding, "Design of near-infrared imaging probe with the assistance of ultrasound localization," *Appl. Opt.* **40**(19), 3288–3303 (2001).
29. Q. Zhu, T. Durduran, V. Ntziachristos, M. Holboke, and A. G. Yodh, "Imager that combines near-infrared diffusive light and ultrasound," *Opt. Lett.* **24**(15), 1050–1052 (1999).
30. B. J. Tromberg, "Optical scanning and breast cancer," *Acad. Radiol.* **12**(8), 923–924 (2005).
31. N. Shah, A. Cerussi, C. Eker, J. Espinoza, J. Butler, J. Fishkin, R. Hornung, and B. Tromberg, "Noninvasive functional optical spectroscopy of human breast tissue," *Proc. Natl. Acad. Sci. U.S.A.* **98**(8), 4420–4425 (2001).
32. T. H. Pham, O. Coquoz, J. B. Fishkin, E. Anderson, and B. J. Tromberg, "Broad bandwidth frequency domain instrument for quantitative tissue optical spectroscopy," *Rev. Sci. Instrum.* **71**(6), 2500–2513 (2000).
33. S. K. No and P. H. Chou, "Mini-FDPM and heterodyne mini-FDPM: handheld non-invasive breast cancer detectors based on frequency domain photon migration," *IEEE Trans. Circuits Syst., I: Fundam.*

- Theory Appl.* **11** (2005).
34. D. B. Jakubowski, A. E. Cerussi, F. Bevilacqua, N. Shah, D. Hsiang, J. Butler, and B. J. Tromberg, "Monitoring neoadjuvant chemotherapy in breast cancer using quantitative diffuse optical spectroscopy: a case study," *J. Biomed. Opt.* **9**(1), 230–238 (2004).
 35. B. Chance, S. Nioka, J. Zhang, E. F. Conant, E. Hwang, S. Briest, S. G. Orel, M. D. Schnall, and B. J. Czerniecki, "Breast cancer detection based on incremental biochemical and physiological properties of breast cancers: A six-year, two-site study," *Acad. Radiol.* **12**(8), 925–933 (2005).
 36. C. Bremer, V. Ntziachristos, and R. Weissleder, "Optical-based molecular imaging: Contrast agents and potential medical applications," *Eur. Radiol.* **13**, 231–243 (2003).
 37. A. Godavarty, A. B. Thompson, R. Roy, M. J. Eppstein, C. Zhang, M. Gurfinkel, and E. M. Sevick-Muraca, "Diagnostic imaging of breast cancer using fluorescence-enhanced optical tomography: phantom studies," *J. Biomed. Opt.* **9**(3), 488–496 (2004).
 38. R. Roy, A. B. Thompson, A. Godavarty, and E. M. Sevick-Muraca, "Tomographic fluorescence imaging in tissue phantoms: A novel reconstruction algorithm and imaging geometry," *IEEE Trans. Med. Imaging* **24**(2), 137–154 (2005).
 39. J. Wu, L. Perelman, R. R. Dasari, and M. S. Feld, "Fluorescence tomographic imaging in turbid media using early-arriving photons and Laplace transforms," *Proc. Natl. Acad. Sci. U.S.A.* **94**, 8783–8788 (1997).
 40. V. Ntziachristos, C. H. Tung, C. Bremer, and R. Weissleder, "Fluorescence molecular tomography resolves protease activity in vivo," *Nat. Med.* **8**, 757–760 (2002).
 41. E. E. Graves, J. Ripoll, R. Weissleder, and V. Ntziachristos, "A sub-millimeter resolution fluorescence molecular imaging system for small animal imaging," *Med. Phys.* **30**, 901–911 (2003).
 42. A. Godavarty, A. B. Thompson, R. Roy, M. Gurfinkel, M. J. Eppstein, C. Zhang, and E. M. Sevick-Muraca, "Diagnostic imaging of breast cancer using fluorescence enhanced optical tomography: phantom studies," *J. Biomed. Opt.* **9**, 488–496 (2004).
 43. A. Godavarty, C. Zhang, M. J. Eppstein, and E. M. Sevick-Muraca, "Fluorescence-enhanced optical imaging of large phantoms using single and simultaneous dual point illumination geometries," *Med. Phys.* **31**, 183–190 (2004).
 44. C. Wu, H. Barnhill, X. Liang, Q. Wang, and H. Jiang, "A new probe using hybrid virus dye nanoparticles for near-infrared fluorescence tomography," *Opt. Commun.* **255**, 366–374 (2005).
 45. G. Zacharakis, J. Ripoll, R. Weissleder, and V. Ntziachristos, "Fluorescent protein tomography scanner for small animal imaging," *IEEE Trans. Med. Imaging* **24**, 878–885 (2005).
 46. A. Godavarty, E. M. Sevick-Muraca, and M. J. Eppstein, "Three-dimensional fluorescence lifetime tomography," *Med. Phys.* **32**, 992–1000 (2005).
 47. Q. Z. Zhang and H. B. Jiang, "Three-dimensional diffuse optical imaging of hand joints: System description and phantom studies," *Opt. Lasers Eng.* **43**, 1237–1251 (2005).
 48. E. E. Graves, R. Weissleder, and V. Ntziachristos, "Fluorescence molecular imaging of small animal tumor models," *Curr. Mol. Med.* **4**(4), 419–430 (2004).
 49. V. Ntziachristos, J. Ripoll, L. H. V. Wang, and R. Weissleder, "Looking and listening to light: the evolution of whole-body photonic imaging," *Nat. Biotechnol.* **23**(3), 313–320 (2005).
 50. B. W. Pogue, S. L. Gibbs, B. Chen, and M. Savellano, "Fluorescence imaging *in vivo*: Raster scanned point-source imaging provides more accurate quantification than broad beam geometries," *Technol. Cancer Res. Treat.* **3**(1), 15–21 (2004).
 51. J. Ripoll and V. Ntziachristos, "Imaging scattering media from a distance: theory and applications of noncontact optical tomography," *Mod. Phys. Lett. B* **18**(28–29), 1403–1431 (2004).
 52. E. M. Sevick and C. L. Burch, "Origin of phosphorescence signals reemitted from tissues," *Opt. Lett.* **19**, 1928–1930 (1994).
 53. M. S. Patterson and B. W. Pogue, "Mathematical model for time-resolved and frequency-domain fluorescence spectroscopy in biological tissues," *Appl. Opt.* **33**, 1963–1974 (1994).
 54. C. L. Hutchinson, J. R. Lakowicz, and E. M. Sevick-Muraca, "Fluorescence life-time based sensing in tissues: A computational study," *Biophys. J.* **68**, 1574–1582 (1995).
 55. F. Fedele, J. P. Laible, and M. J. Eppstein, "Coupled complex adjoint sensitivities for frequency-domain fluorescence tomography: Theory and vectorized implementation," *J. Comput. Phys.* **187**, 597–619 (2003).
 56. J. M. Schmitt, A. Knüttel, and J. R. Knutson, "Interference of diffusive light waves," *J. Opt. Soc. Am. A* **9**, 1832–1843 (1992).
 57. A. Knüttel, J. M. Schmitt, and J. R. Knutson, "Spatial localization of absorbing bodies by interfering diffusive photon-density waves," *Appl. Opt.* **32**, 381–389 (1993).